Drive Cycle-Based Accelerated Stress Tests for Heavy Duty Fuel Cell Vehicle Applications

Citation for the original published paper (version of record):
Kothala, G., Sedarsky, D., Haberl, F. et al (2026). Drive Cycle-Based Accelerated Stress Tests for Heavy Duty Fuel Cell Vehicle Applications. Fuel Cells, 26(3). http://dx.doi.org/10.1002/fuce.70108

Fuel Cells

RESEARCH ARTICLE OPEN ACCESS

Drive Cycle-Based Accelerated Stress Tests for Heavy Duty Fuel Cell Vehicle Applications

Gnana Lahari Kothala[1,2] | David Sedarsky[1] | Felix Haberl[2] | Gustavo Hindi[2]

[1]Department of Mechanics and Maritime Sciences, Chalmers University of Technology, Göteborg, Sweden | [2]Powertrain Strategic Development, Volvo Group Trucks Technology, Göteborg, Sweden

Correspondence: Gnana Lahari Kothala (lahari@chalmers.se)

Received: 14 October 2025 | **Revised:** 1 April 2026 | **Accepted:** 6 May 2026

Keywords: accelerated stress tests | AST | drive cycle | fuel cell | heavy-duty vehicle

ABSTRACT

Fuel cells in heavy-duty vehicles are susceptible to degradation and are significantly influenced by driving patterns. Accelerated stress tests (ASTs) are useful to identify these degradation mechanisms and aid the development of degradation-resistant control strategies for FC stacks. Conventional ASTs are designed to address material degradation over time, but the dynamic stresses encountered by the fuel cell during real-world driving occur under different operating conditions. This work proposes an algorithm to generate a drive cycle-based AST to face this challenge and provides an efficient method for assessing fuel cell durability. Our method incorporates voltage cycling, high load operation, and idling periods, weighted to reflect the distribution of these conditions for a specific drive cycle. The formulated ASTs are given as inputs to a one-dimensional catalyst layer degradation model, which estimates the loss of electrochemical surface area (ECSA) based on platinum (Pt) oxidation, Pt dissolution, Pt particle size distribution, and carbon corrosion. A postmortem analysis of single cells, exploiting identical location-transmission electron microscopy (IL-TEM), was performed to investigate the underlying degradation processes and validate the accuracy of the modeling outcomes. Good agreement was observed between the model and experimental data, demonstrating the predictive capability for ECSA loss across a range of cell temperatures and relative humidity levels. Comparing the generated ASTs and representative drive cycle degradation characteristics, it is evident that a similar amount of ECSA loss can be achieved in a significantly shorter period. In addition, we demonstrate an accelerated degradation algorithm capable of simulating long-term fuel cell degradation, producing ASTs that are representative of real-world driving conditions.

1 | Introduction

Current proton exchange membrane fuel cell lifetime targets aim for over 8000 h for passenger car applications and 30 000 h for heavy-duty vehicles, with Japan's new energy and industrial technology development organization (NEDO) setting an ambitious goal of 50 000 h for heavy-duty applications [1]. To verify these lifetime targets, continuous monitoring and validation of fuel cell performance over extended operating periods are needed, entailing significant time and cost commitments. To reduce the test duration and estimate the lifetime in short periods, accelerated stress tests (ASTs) play a crucial role by simulating operating conditions to identify degradation pathways, assessing material durability, and operational strategies [2]. The lifespan of a fuel cell depends on various operating conditions and driving patterns, and the underlying degradation mechanisms can be attributed to multiple factors, including membrane degradation, platinum (Pt) oxidation, dissolution, particle size distribution (PSD), and carbon corrosion [3]. Extensive research has been conducted on degradation analysis methods and mitigation strategies to enhance the lifetime of PEMFCs in automotive applications [4, 5]. The US Department of Energy (DOE) has established standardized AST protocols to evaluate the durability of PEMFC components. These include potential cycling tests for platinum stability (0.6–0.95 V) under high temperatures (80°C) and 100% relative humidity (RH) conditions, as well as carbon corrosion assessments through potential cycling (1–1.5 V) under similar environmental conditions [6–9]. In addition, membrane durability is assessed using mechanical and chemical ASTs, subjecting the membrane to high potential ($\geq$ 1.4 V) and RH cycling or elevated temperatures to trigger mechanical failure through swelling/shrinking of the membrane [10, 11]. Chemical degradation is induced under steady-state open-circuit voltage (OCV) or through combined OCV and RH cycling protocols. These AST procedures are frequently modified by adjusting operating parameters such as temperature, humidity, dwell times, and ramp rates to accelerate specific degradation modes. Most of the published ASTs employ potential cycling between an upper potential limit (UPL) and a lower potential limit (LPL), with the LPL typically set at 0.6 V and UPL values ranging from 0.9, 0.95, 1 V to as high as 1.5 V [12–15], to promote catalyst corrosion [16]. Many researchers have extended their work to encompass AST methodologies for overall membrane electrode assembly (MEA), aiming to better represent system-level degradation and thereby improve PEMFC reliability and durability [17, 18].

While these conventional ASTs are effective in addressing material degradation and accelerating test durations, they may not fully replicate the complex degradation that occurs in PEMFCs under real-world driving conditions [19]. Dynamic stressors such as voltage cycling, temperature fluctuations, and humidity variations impose operating conditions that differ significantly from conventional AST protocols. As a result, accurately capturing their distinct degradation effects remains a challenge [20]. Schüttoff et al. conducted an extensive investigation to align accelerated durability tests (ADTs) with conditions representative of real-world fuel cell operation [21]. Long-term stack testing was performed to assess lifetime under these protocols. Their findings indicated that the strongest acceleration effects occurred in the mass transport regime when RH was employed as a primary stressor. However, the implementation of voltage clipping significantly suppressed catalyst layer (CL) degradation, thereby limiting the ADT's ability to capture degradation pathways associated with voltage cycling. This limitation underscores the necessity of developing drive cycle-based AST protocols that more accurately replicate dynamic operating conditions and capture the full spectrum of degradation mechanisms. Moreover, vehicle-specific driving conditions, such as regional haul vehicles, operate over short to medium distances with frequent stops, acceleration, and idling. In contrast, long-haul vehicles operate over extended distances with high load operation and minimal stops, influencing the degradation of the fuel cell [22]. These different driving patterns influence the degradation mechanisms, highlighting the necessity for a drive cycle-based AST to optimize the fuel cell performance.

This work focuses on developing drive cycle-based AST protocols for fuel cells by identifying key driving scenarios, such as high load, dynamic load, and idle, within the drive cycle. A detailed degradation model is used to understand and compare the voltage drop in different scenarios. Mayur et al. proposed a multi-scale framework that connects a vehicle-level fuel cell model with a cell-level catalyst degradation sub-model, enabling customization using real-world drive cycle data [23]. However, its predictive capability is constrained, as it does not incorporate the influence of voltage cycling on platinum stability. The degradation factor used in this methodology is empirical, which limits its transferability across operating conditions. In particular, the aggregation of multiple degradation processes into a single factor restricts the generalizability of such models and reduces their effectiveness under diverse load profiles and environmental conditions. Kneer et al. introduced a semiempirical framework that utilizes AST data to predict platinum surface area loss during voltage cycling [24]. This model was further integrated with an analytical polarization curve representation to estimate the corresponding performance of the MEA. While effective in scenarios where platinum dissolution and particle growth dominate, its applicability is limited when additional degradation phenomena are present. Establishing a direct relationship between the PSD and electrochemical surface area (ECSA) is critical for achieving accurate durability predictions and for integrating multiple degradation mechanisms within a unified catalyst model. In the current work, we employ a one-dimensional CL degradation modeling based on the thermokinetic equations and nonuniform platinum (Pt) degradation distributed across the cathode CL as developed by Holby et al. The model tracks the rate of Pt oxidation, dissolution, PSD, and carbon corrosion and estimates the overall ECSA loss over time. To validate the accuracy and effectiveness of the developed AST approaches, the model predictions are compared to experimental results obtained through analysis with identical location-transmission electron microscopy (IL-TEM). This comparison helps to ensure that the devised AST methods accurately reflect the real-world performance and degradation behaviors of fuel cells under the tested operating conditions.

The structure of this paper is outlined as follows: Section 2 discusses the degradation mechanisms of the CL and outlines the fundamental equations utilized for modeling. Section 3 details the development of the AST algorithm, which is formulated based on vehicle operation characteristics and rain flow analysis techniques. Section 4 discusses the degradation model validation with experimental results and the AST outcomes across various drive cycle scenarios. Finally, Section 5 provides a summary of findings and concluding remarks.

2 | Degradation Mechanisms and Modeling

The fuel cell consists of multiple layers, including bipolar plates (BPPs), a CL, a gas diffusion layer (GDL), a membrane, and others. The CL consists of platinum nanoparticles dispersed on a carbon (C) support, which provides a high surface area for catalytic reactions. The ionomer, typically Nafion, surrounds the catalyst particles, facilitating proton conductivity while maintaining electrical insulation. The Pt/C structure ensures efficient electron transport and reaction kinetics, while the ionomer optimizes proton accessibility to reaction sites. This combination is crucial for enhancing fuel cell performance and durability. However, understanding the degradation of the CL is vital

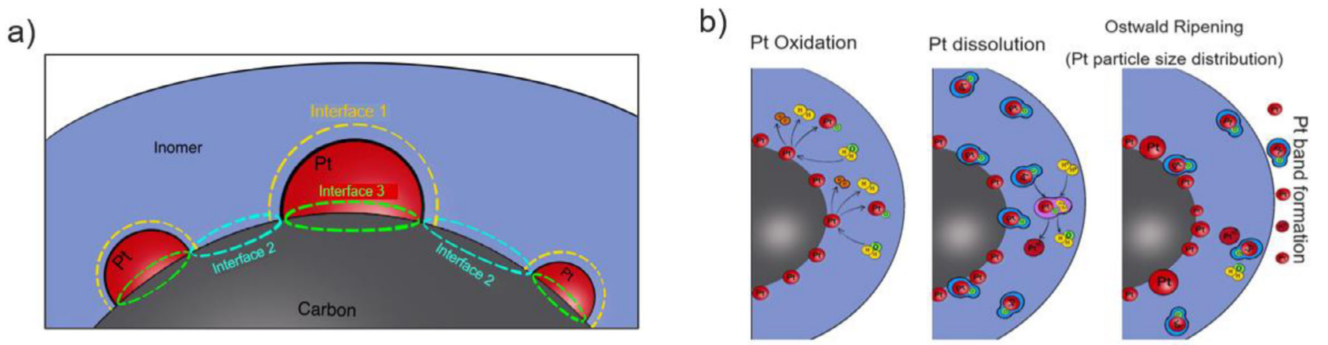

FIGURE 1 | The catalyst layer structure is shown in the left image with three microscopic interfaces: Interface 1—Pt–ionomer interactions, Interface 2—carbon–ionomer interactions, and Interface 3—Pt–carbon interactions. The right image shows different Pt electrochemical reactions, which cause degradation in the CL.

to improving fuel cell efficiency and longevity. To investigate the degradation mechanisms and their impact on the overall performance of the fuel cell, we divided the CL into three different microscopic interfaces, as shown in Figure 1. The degradation phenomena associated with each interface were analyzed and incorporated into the modeling framework. At Interface 1 (Pt–ionomer), platinum oxide (PtO) formation is observed, influencing the electrochemically active surface area and reaction kinetics. At Interface 2 (carbon–ionomer), the carbon support is susceptible to electrochemical oxidation, leading to carbon corrosion and structural degradation. At Interface 3 (Pt–carbon), degradation is dominated by platinum dissolution and Ostwald ripening on the carbon surface, resulting in particle growth and loss of active surface area. All these mechanisms are studied in detail further and modeled.

2.1 | Platinum Degradation

The main mechanisms of Pt degradation, as shown in Figure 1b, are oxidation, dissolution, redistribution of particle size through Ostwald ripening of the Pt particles on the carbon support, and agglomeration of Pt nanoparticles due to carbon corrosion [25]. When the Pt nanoparticle reacts with a water molecule, PtO is formed, limiting the availability of the Pt surface to support the oxygen reduction reaction (ORR).

$$\mathrm{Pt} + \mathrm{H2O} \rightarrow \mathrm{PtO} + \mathrm{2H+} + 2\mathrm{e}^{-} \tag{1}$$

$$\mathrm{Pt} \rightarrow \mathrm{Pt2+} + 2\mathrm{e}^{-} \tag{2}$$

The chemical dissolution of PtO, which has slow reaction kinetics, is assumed to be negligible in this model. Platinum dissolution occurs under dynamic potential conditions, where Pt dissolves into the ionomer and migrates. This leads to the thinning of the CL and redeposition on the Pt particles, contributing to agglomeration. The dissolved Pt^{2+} ions form a Pt band at the CL-membrane interface. Holby and Morgan developed a thermokinetic rate model, which describes the rate of PtO formation and the rate of Pt dissolution [26]. Here, the rate of forward and backward reactions is given by the Eyring–Polanyi equation [27]. The net rate of Pt oxidation ($r_{\mathrm{net,\,oxide}}$) and the net rate of Pt dissolution ($r_{\mathrm{net,\,Pt}}$) are described by Equations (3) and (4), respectively. A detailed discussion can be found in [28].

$$r_{\mathrm{net,oxide}} = \upsilon_1^{*}\,\Gamma\,\exp\left[\frac{-1}{RT}\left(\overleftarrow{H}_{2,\mathrm{fit}} + \lambda\theta_{i,j}\right)\right] \times \left(\begin{array}{l} \left(1 - \frac{\theta_{i,j}}{2}\right)\exp\left[-\frac{n_2F(1-\beta_2)}{RT}\left(U_{\mathrm{fit}} + \frac{\omega\theta_{i,j}}{n_2F} - V\right)\right] \\ -\frac{\upsilon_2^{*}}{\upsilon_1^{*}}\left(10^{-2\mathrm{pH}}\right)\exp\left[\frac{n_2F\beta_2}{RT}\left(U_{\mathrm{fit}} + \frac{\omega\theta_{i,j}}{n_2F} - V\right)\right] \end{array}\right) \tag{3}$$

$$r_{\mathrm{net,Pt}} = \upsilon_1\Gamma\exp\left[\frac{-\bar{H}_{1,\,\mathrm{fit}}}{RT}\right]\left(1 - \min\left(1, \theta_{i,j}\right)\right) \times \left(\begin{array}{c} \exp\left[-\frac{nF(1-\beta_1)}{RT}\left(U_{\mathrm{eq}} - \frac{4\Omega\gamma_{\mathrm{total}}}{d_{i,j}nF} - V\right)\right] \\ -\frac{\upsilon_2}{\upsilon_1}\frac{c_{\mathrm{Pt}^{2+}}^{\mathrm{ref}}}{c_{\mathrm{Pt}2}^{\mathrm{r}2}}\exp\left[\frac{nF\beta_1}{RT}\left(U_{\mathrm{eq}} - \frac{4\Omega\gamma_{\mathrm{total}}}{d_{i,j}nF} - V\right)\right] \end{array}\right) \tag{4}$$

where the total surface tension γ (J/cm^2) can be described as:

$$\gamma_{\mathrm{total}} = \gamma + \Gamma\theta_{\mathrm{i,j}}RT \times \left[\log\left(\frac{\upsilon_2}{\upsilon_1^{*}}\right) + \log\left(10^{-2\mathrm{pH}}\right) + \frac{n_2F}{RT}\left(U_{\mathrm{fit}} - V\right) + \frac{\omega\theta_{\mathrm{i,j}}}{2RT} + \log\left(\frac{\theta_{\mathrm{i,j}}}{2}\right) + \frac{2-\theta_{\mathrm{i,j}}}{\theta_{\mathrm{i,j}}}\log\left(\frac{1-\theta_{\mathrm{i,j}}}{2}\right)\right] \tag{5}$$

In addition, particle growth through Ostwald ripening and coalescence leads to a loss of active surface area, as smaller Pt particles dissolve and redeposit onto larger ones or merge. In this model, for each particle size class (i, j), both the particle diameter evolution and the corresponding oxide coverage are monitored over time. The initial number of particles within a given size group is obtained from the prescribed PSD and the total particle count, which is calculated based on the mean particle diameter d, electrode area, and platinum loading. At the beginning of the simulation, the oxide fractional coverage $\theta_{i,j}$ for all particle groups is set to zero. The temporal evolution of the particle diameter is then described by a rate expression with units of (cm/s).

$$\frac{d\left(\theta_{i,j}\right)}{dt} = \frac{r_{\mathrm{net,oxide}}}{\Gamma} - \frac{2\theta_{\mathrm{i,j}}}{d_{\mathrm{i,j}}}\frac{d\left(d_{i,j}\right)}{dt} \tag{6}$$

$$\frac{d\left(d_{i,j}\right)}{dt} = -r_{net,Pt}\Omega \tag{7}$$

2.2 | Carbon Corrosion

Carbon corrosion primarily occurs due to the oxidation of the carbon support at high potentials or temperatures, negatively affecting performance and durability. When the carbon support reacts with water, carbon dioxide and carbon monoxide are formed, as shown in Equations (8) and (9). The kinetic model proposed by Gallagher and Fuller [29] is employed in this work, which captures the formation of CO_2 and intermediate surface carbon oxides, enabling the prediction of electrode response, carbon mass loss, and surface oxide growth as functions of operating time, temperature, and applied potential during the electrochemical oxidation of graphitic carbon [30, 31].

$$\mathrm{C + H2O \rightarrow CO + 2H+ + 2e^{-}} \tag{8}$$

$$\mathrm{C + 2H2O \rightarrow CO2 + 4H+ + 4e^{-}} \tag{9}$$

The rate of formation of carbon dioxide and carbon monoxide can be expressed as:

$$r_1 = k_1\,\theta_{\mathrm{vac}} \exp\left[\frac{\alpha_1 F}{RT}\left(V - U_1\right) - g\theta_{C\#OH}\right] \tag{10}$$

$$r_2 = k_2\theta_{\mathrm{vac}}\theta_{\mathrm{C\#OH}}\left(\frac{p_0}{p_0^{\mathrm{ref}}}\right)\exp\left[\frac{\alpha_2 F}{RT}\left(V - U_2\right)\right] \tag{11}$$

A significant amount of carbon mass is lost due to corrosion reactions. To estimate the carbon loss (N_c), the mass balance equations yield the instantaneous rate of change of carbon mass, given by Equation (12).

$$\frac{d\left(N_{\mathrm{C}}\right)}{d\left(t\right)} = -r_2 SMN_{\mathrm{C}} \tag{12}$$

The electrochemically active surface area (ECSA) and geometric surface area (GSA) were determined using Equations (13) and (14). Since the entire GSA is not accessible for hydrogen adsorption, a scaling factor is required when comparing GSA with the surface area derived from hydrogen adsorption measurements, that is, the ECSA. This scaling factor is established by correlating the GSA obtained from transmission electron microscopy analysis with the ECSA measured via CV. Here, it is assumed that the ratio ECSA(t)/GSA(t) or the scaling factor remains constant throughout the degradation process. Therefore, once GSA(t) is obtained at each time step, the normalized surface area, expressed as ECSA(t)/ECSA(0), can be evaluated. Since these formulations are primarily dependent on platinum particle diameter, the effect of carbon corrosion is incorporated by multiplying ECSA(t) with the fraction of carbon mass loss. Following the same approach, the normalized spatially resolved distribution of surface area can be expressed as ECSA(x, t)/ECSA(x, 0).

$$\mathrm{GSA} = 2\pi \sum_{i=1,j=1}^{N,M} \mathrm{Num}_{i,j}\left(\frac{d_{i,j}}{2}\right)^2 \tag{13}$$

$$\frac{\mathrm{ECA}\left(t\right)}{\mathrm{GSA}\left(t\right)} = \frac{\mathrm{ECA}\left(0\right)}{\mathrm{GSA}\left(0\right)} \tag{14}$$

3 | AST Algorithm and Drive Cycle Optimization

Various methodologies have been proposed in the literature to develop realistic ASTs, most of which aim to capture the key features of real-world driving conditions. The ID-Fast project introduced an AST protocol tailored for automotive fuel cell stacks consisting of two distinct segments: a low-power phase that replicates start–stop operation characterized by low current density and high electrode potential and a high-power phase associated with elevated current load and reduced potential [32, 33]. However, its applicability remains limited to a specific operating scenario. Since vehicle driving profiles vary significantly with route characteristics, the development of use case-dependent drive cycle ASTs is essential to represent real-world degradation phenomena more accurately. Thiele et al. proposed an algorithm for constructing realistic ASTs derived from actual vehicle driving scenarios, thereby aiming to improve the representativeness of laboratory testing [34]. This methodology was primarily based on semiempirical fitting at voltage cycling, high load, and idling, which enabled practical implementation but inherently restricted the model's capability compared to physics-based approaches. This limitation was evident in their results, where the degradation trends captured by the algorithm showed partial agreement with experimental observations. In this study, two distinct approaches are explored for deriving AST profiles, as illustrated in Figure 2. The first approach focuses on directly mapping vehicle operating scenarios, such as dynamic loading, peak power demands, and idling phases, into a stress profile. These driving conditions are extracted and filtered from real-time vehicle data to devise a proportional AST, as detailed in Section 3.1. The second approach employs a statistical technique, the rain flow counting method, to analyze the drive cycles. This method facilitates the derivation of a normalized AST by quantifying the load variation patterns and fatigue-relevant characteristics present in the driving data. An explanation of this methodology is provided in Section 3.2. The drive cycle-based ASTs are constructed under the assumption that the fuel cell operates at a constant temperature of 80°C and 100% RH. This simplification was initially adopted to isolate and evaluate the influence of voltage fluctuations on system degradation. However, the developed degradation model is sufficiently versatile to capture degradation phenomena under varying temperature and humidity conditions, which can be incorporated in future AST formulations.

3.1 | AST Based on Vehicle Operating Conditions

3.1.1 | Dynamic Load

During dynamic load operation, fuel cell parameters such as voltage, temperature, and humidity exhibit continuous fluctuations. Variations in temperature and humidity primarily contribute to the mechanical degradation of the membrane and ionomer structure [35]. The present study emphasizes the degradation of the CL, with a particular focus on voltage-induced effects. Voltage cycling is a key stressor in CL degradation, where electrochemical phenomena such as platinum dissolution and Ostwald ripening are predominantly observed. These mechanisms contribute significantly to the loss of the electrochemically active surface area of Pt particles, thereby impacting cell performance. It is understood

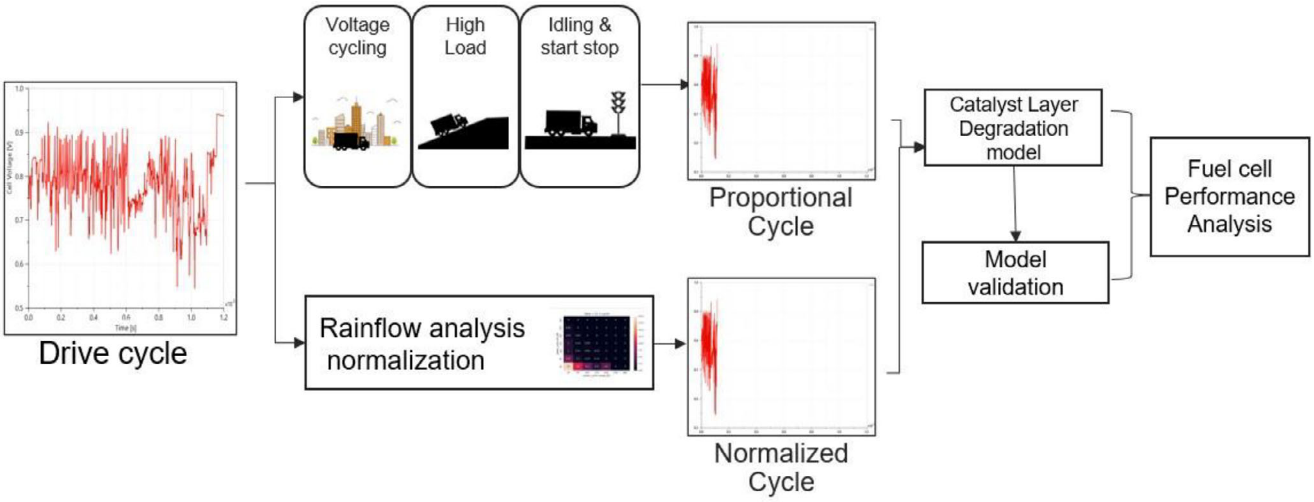

FIGURE 2 | The illustrated methodology translates real-world drive cycle data into two ASTs by filtering based on operation conditions and rain flow cycle counting. The ASTs were compared with the original drive cycle using a catalyst layer degradation model to analyze the fuel cell performance.

that the extent of CL degradation is highly sensitive to parameters such as the upper and lower voltage limits, dwell time at each potential, and scan rate of voltage transitions [36]. To ensure that these degradation-driving parameters closely reflect actual vehicle drive cycles, a CL degradation model was employed to estimate localized degradation throughout the cycle. By analyzing the time-resolved behavior of Pt dissolution and mean Pt particle growth, regions within the drive cycle that exceeded threshold values are identified. These critical segments, where degradation mechanisms are most active, are then selectively integrated into the formulation of the proportional AST profile.

3.1.2 | Idling and Start-Stop Conditions

Similar to dynamic load conditions, idling phases in fuel cell operation also contribute to component degradation. During idling, the fuel cell operates at low current densities, which can lead to uneven voltage distribution across the CL, localized hotspots, reduced water production, and elevated gas partial pressures. These conditions promote the formation of reactive oxygen species, particularly hydrogen peroxide (H_2O_2) and fluoride emissions, which can further accelerate membrane chemical degradation [37, 38]. Researchers are trying to control membrane chemical degradation with proper water management conditions. The model also has a dependency on the load and mass flow rates, which leads to mass transport limitations at low loads. These limitations can exacerbate local oxygen starvation, leading to carbon corrosion in the catalyst support [39, 40]. Moreover, both idling and frequent start-stop events lead to sustained high cathode potential. Start–stop events impose even harsher transients: during startup, air–fuel mixing at the anode can cause severe potential derivations, generate local hot spots, and drive rapid carbon oxidation [41]. Similarly, during shutdown, reverse current phenomena occur due to uneven fuel distribution across the stack, subjecting localized regions to high cathode potentials that accelerate catalyst dissolution and carbon corrosion. Collectively, these operating conditions contribute to the structural instability of the CL and loss of hydrophobicity in gas diffusion media, thereby increasing the mass transport resistance; simultaneously, the formation of unsupported or agglomerated particles raises the charge transfer resistance, disrupting the three-phase boundary essential for effective electrochemical reactions. Collectively, these phenomena contribute to a substantial decline in the ECSA, compromising the overall fuel cell performance and durability.

3.1.3 | Full Power/High Load

High load operating conditions in fuel cells are characterized by low cell voltages and elevated water production due to increased electrochemical activity. Excessive water generation under these conditions can result in cathode flooding, which compromises the cell mass transport characteristics [42]. Flooding leads to the displacement and eventual degradation of the polytetrafluoroethylene (PTFE) hydrophobic layer, thereby increasing the risk of carbon support corrosion and further elevating mass transfer resistance [5, 43]. In addition, the accumulation of water can cause gas starvation, particularly oxygen deficiency at the cathode, which accelerates performance degradation and contributes to ECSA loss. Another critical factor under high load and low voltage operation is ionomer dissolution. At such low potentials, the ionomer within the CL becomes unstable, resulting in a loss of ionic conductivity and further reduction in ECSA. However, ionomer degradation is not accounted for in this model. These high-load events have been captured within the dynamic load operational scenarios, as they inherently include prolonged exposure to lower voltage levels.

These segments, where the degradation is beyond the threshold limits ($> 90\%$), are extracted to incorporate the impact of high-load conditions into the overall degradation model and the development of representative AST protocols. All segments of the drive cycle that exceeded predefined limits are identified, filtered, and consolidated. These critical segments are then merged and structured into a proportional AST that effectively replicates the degradation behavior of the original drive cycle within a reduced time.

3.2 | Rain Flow Analysis Method

The rain flow counting method [44] is utilized to systematically quantify both the number and magnitude of load fluctuations occurring at each point within the drive cycle. Originally developed as a cycle counting algorithm in mechanical fatigue analysis, rain flow analysis is designed to identify and categorize stress reversals by decomposing complex, irregular load profiles into a series of simple, individual load cycles. This process involves tracking the peaks and valleys in the load data, which allows for an accurate assessment of cyclic stress and the potential accumulation of fatigue damage over time. The MATLAB rainflow counting function is used to analyze the drive cycle data. The algorithm preprocesses the signal by retaining only the local maxima and minima (peaks and valleys) to reduce data complexity while preserving the essential load variations. The rainflow algorithm then identifies full cycles, half cycles, and their respective counts, along with the corresponding start and end points of each fluctuation. In addition, the function computes the mean value and range for each identified fluctuation, which can be used for degradation assessment.

In this study, this technique is adapted to analyze the fluctuation in the voltage profile of a fuel cell operating with a real-time driving scenario. To create an AST from a voltage profile, the key parameters are the voltage range and the scan rate. By applying the rainflow algorithm, the start and end points of each voltage fluctuation are identified, enabling the extraction of the corresponding voltage range (i.e., minimum and maximum voltage), and the scan rate of each fluctuation is calculated. Then, the voltage transitions are discretized into bins according to their cycle minimum and scan rates, resulting in the construction of a rainflow matrix. This matrix provides a comprehensive representation of the voltage fluctuation characteristics over the entire drive cycle. To generate an AST profile while capturing the representative behavior of the driving pattern, the frequency of voltage fluctuations within each bin is normalized as per Equation (15). When the number of fluctuations in the given bin (N_{cycle}) are greater than the normalization factor (k), then the total number of occurrences is divided by this factor to generate a new bin with a reduced count of fluctuations (N_{AST}) used for creating the normalized cycle. In contrast, if the fluctuation count is less than or equal to the normalization factor, the bin remains unchanged. This normalization process reduces the number of fluctuations in each bin while maintaining the extreme events of the cycle. This results in a simplified yet dynamically equivalent stress cycle that encapsulates the essential features of the original drive cycle.

$$N_{AST} = \begin{cases} N_{cycle}/k & \text{If } N_{cycle} > k \\ N_{cycle} & \text{If } N_{cycle} \leq k \end{cases} \tag{15}$$

Furthermore, this normalized cycle retains critical characteristics such as voltage sweep rates and the distribution of operating time across high and low potential regions. These features are particularly important because they are linked to key electrochemical degradation mechanisms in fuel cells, including platinum dissolution and carbon corrosion. By preserving these aspects, the method provides an understanding of predicting the long-term durability and performance of fuel cells under heavy-duty vehicle applications.

4 | Discussion and Results

4.1 | Degradation Model Validation

The degradation model used in this study is formulated based on the electrochemical and physical mechanisms described in Section 1. Based on the input voltage profile, the model simulates the degradation processes, which are closely linked to the dynamic voltage fluctuations encountered during fuel cell operation. To validate the model predictions, experimental studies were performed on a 5 cm^2 single cell incorporating a three-layer catalyst-coated membrane with platinum loadings of 0.1 $\mathrm{mgPt/cm}^2$ on the anode and 0.4 $\mathrm{mgPt/cm}^2$ on the cathode. The test bench, designed in-house, supplied reactant gases via heated humidification bottles with flow rates precisely regulated using mass flow controllers. Electrochemical measurements were conducted with a potentiostat, including cyclic voltammetry (CV) performed between 0.07 and 1.0 V at a scan rate of 50 mV/s under operating conditions of 80°C and with gas flows of 20/5 nccm hydrogen (H_2)/argon (Ar) (anode/cathode). The hydrogen adsorption region in the CV was used to determine the electrochemically active surface area after subtracting contributions from the double-layer capacitance. A square wave AST profile is executed, which is voltage cycling between 0.6 and 1.0 V, with 8-s hold times at each potential, under operating conditions of 80°C and 100% RH. At the beginning of the AST and following every 5000 cycles, the MEA was extracted for IL-TEM analysis. To ensure reproducible imaging, the cathode GDL was removed, and the MEA was mounted in a custom-built TEM holder with coordinate-based tracking, enabling repeated imaging of the same CL location without physical marking. The cathodic CL was examined at an accelerating voltage with identical working distance settings across all imaging sessions. After TEM analysis, the GDL was repositioned, and the MEA reassembled into the test cell, as outlined in [45]. These combined electrochemical and microstructural characterizations were employed to track the platinum PSD and ECSA evolution, thereby providing quantitative insights into catalyst degradation under controlled AST conditions.

Based on the CV measurements, a set of model parameters that are dependent on the cell characteristics was calibrated for this test cell. Since several parameters in the model are dependent on cell-specific characteristics, their values must be adjusted accordingly to ensure an accurate representation of the system. The fitted parameters include the partial molar activation enthalpy for oxide formation at zero coverage, $\overset{\}}{H}_{2,\mathrm{fit}}$, which was adjusted from 1.2×10^4 to 9.0×10^4 J/mol. The bulk equilibrium potential for Pt oxide formation, U_{fit}, was modified from 1.03 to 0.4 V. The reference Pt^{2+} concentration was updated from 4.0×10^{-3} to 1.0×10^3 mol/L. In addition, the activation enthalpy for Pt dissolution under fully humidified conditions, $\overset{\}}{H}_{1,\mathrm{fit}}$, was adjusted from 4.0×10^4 to 4.79×10^4 J/mol. The calibrated parameter values are summarized in Table 1. It should be noted that these parameters are not constants, as mentioned in references [27, 28], and must be recalibrated for the cell. Following calibration,

TABLE 1 | List of physical properties and parameters used in the CL degradation modeling.

Symbol	Description	Value	Units	Refs.
υ_1^*	Forward Pt oxide formation rate constant	1×10^4	Hz	[28]
υ_2^*	Backward Pt oxide formation rate constant	2×10^{-2}	Hz	[28]
Γ	Pt surface site density	2.2×10^{-9}	mol/cm^2	[28]
$\overleftharpoondown{H}_{2,\text{fit}}$	Partial molar oxide formation activation enthalpy (zero coverage)	9×10^4	J/mol	Fit
β_2	Butler–Volmer transfer coefficient for Pt oxide formation	0.5	—	[28]
n_2	Electrons transferred during Pt oxide formation	2		[28]
U_{fit}	Pt oxide formation bulk equilibrium voltage	0.4	V	Fit
λ	Pt oxide-dependent kinetic barrier constant	2.0×10^4	J/mol	[28]
ω	Pt oxide–oxide interaction energy	5.0×10^4	J/mol	[28]
ν_1	Dissolution attempt frequency	1×10^4	Hz	[28]
ν_2	Backward dissolution rate factor	8×10^5	Hz	[28]
β_1	Butler–Volmer transfer coefficient for Pt dissolution	0.5		[28]
n	Electrons transferred during Pt dissolution	2		[28]
U_{eq}	Pt dissolution bulk equilibrium voltage	1.118	V	[28]
Ω	Molar volume of Pt	9.09	cm^3/mol	[28]
γ	Pt (111) surface tension	2.4×10^{-4}	J/cm^2	[28]
C_{ref}	Reference Pt^{2+} concentration	1×10^3	mol/L	Fit
$\bar{H}_{1,\text{ fit}}$	Pt dissolution activation enthalpy under fully humidified conditions	4.79×10^4	J/mol	Fit
k_1	Reaction rate constant of Step 1	2.35×10^{-16}	mol/cm^2 s	[31]
k_2	Reaction rate constant of Step 2	9.5×10^{-13}	mol/cm^2 s	[31]
α_1	Transfer coefficient of Step 1	0.35		[31]
α_2	Transfer coefficient of Step 2	0.65		[31]
U_1	Equilibrium potential of Step 1	1	V	[31]
U_2	Equilibrium potential Step 2	0.15	V	[31]
g	Frumkin factor	3		[31]
S	Specific surface area	1×10^4	cm^2/g	[31]
M	Molecular weight of carbon	12	g	[31]

the fuel cell model is simulated under the AST profile, and the mean Pt particle diameter and ECSA results are compared with experimental data for validation.

As shown in Figure 3, the simulated evolution of the mean platinum particle diameter demonstrates good agreement with the experimental data, with deviations remaining within 1%–2% throughout the test. A pronounced decrease in ECSA was observed experimentally after the initial 5000 cycles, which appeared anomalous during the experimental data analysis. The physics-based model, however, successfully captured this sharp initial loss by accounting for carbon mass loss occurring in the initial stages of the AST. This indicates the model's capability to estimate the degradation and provide insights that are difficult to extract from experiments alone. It is important to note that this rapid initial drop is strongly dependent on the specific MEA chemistry used in this study and may not necessarily manifest in other MEA configurations. Overall, the close agreement between the simulated and measured mean particle diameters underscores the robustness of the model in reproducing both catalyst degradation and support-related effects under realistic operating conditions.

4.2 | Degradation of Devised ASTs

The developed degradation model was further applied to evaluate regional-haul and long-haul drive cycles. Regional-haul vehicles typically operate over short to medium distances and are characterized by frequent stopping, acceleration, and idling events. In contrast, long-haul vehicles are operated over extended distances under sustained high-load conditions with minimal interruptions. These distinct duty cycles influence fuel cell degradation behavior, leading to different dominant degradation mechanisms and rates under regional and long-haul operating conditions. As outlined in Section 3, both proportional and normalized AST representations were derived for these two operating profiles, and their outcomes are summarized in Table 2.

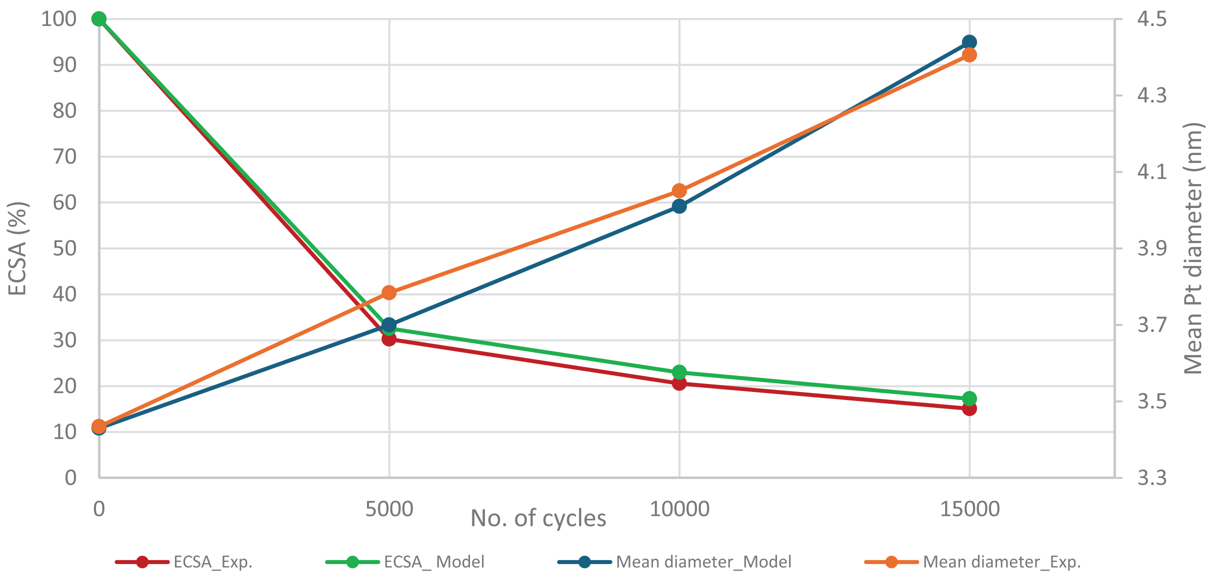

FIGURE 3 | Comparison of simulation and experimental results of mean Pt particle diameter and percentage of ECSA for every 5000 cycles. The blue line indicates the simulation mean Pt diameter; the orange line indicates the experimental mean Pt particle diameter. The green line shows the ECSA percentage with simulation, and the red line shows the ECSA percentage with experiments.

TABLE 2 | The cycle duration and ECSA loss (cm^2/mg Pt) after testing for 100 h with the drive cycle, proportional cycle, and normalized cycle under different driving scenarios (regional and long haul).

	Regional haul	Long haul	Regional haul		Long haul	
			ECSA (cm^2/mg Pt) after 100 h of testing			
	Cycle duration		BOT	EOT	BOT	EOT
Drive cycle	221 min	650 min	261.7	251.7	261.7	259.3
Proportional cycle	51 min	99 min	261.7	235.7	261.7	255.7
Normalized cycle	32 min	99 min	261.7	228.7	261.7	254.3

The results demonstrate that the devised ASTs are capable of significantly accelerating the degradation processes relative to the original drive cycles. For the regional-haul cycle, the total simulation time was reduced by approximately 76% using the proportional AST and by nearly 85% using the normalized AST. The degradation trends reflect the operational characteristics of regional-haul duty, which involves less idling and more potential cycling. These conditions accelerate carbon corrosion, leading to measurable carbon mass loss and distinct shifts in the platinum PSD. Quantitatively, approximately 4% of the overall degradation is attributable to idling, while approximately 20% results from voltage cycling events, as illustrated in Figure 4. When comparing ECSA losses, both proportional and normalized ASTs produced an acceleration factor of two relative to the baseline cycle, confirming that the same driving events induce faster degradation under the AST framework. These findings highlight the ability of AST methodologies to reproduce representative degradation modes while reducing experimental time requirements for regional-haul drive cycle analysis.

For the long-haul drive cycle, the application of both proportional and normalized AST approaches reduced the overall simulation duration by nearly 85%, thereby enabling accelerated evaluation of durability impacts. Unlike regional-haul operation, the long-haul profile is dominated by steady highway driving, with cell voltages confined to a narrow range of 0.72–0.76 V. This moderate potential regime is associated with reduced degradation severity compared to highly transient duty cycles. Nevertheless, the long-haul cycle is not degradation-free; few idling events and the presence of high cathode potentials introduce additional stressors that trigger mechanisms such as carbon corrosion and platinum dissolution. The resulting degradation pattern is therefore a combination of contributions from both high-potential idling and moderate voltage cycling. Quantitative analysis indicates that idling-related segments contribute approximately 8% of the total degradation, while voltage cycling accounts for a similar fraction (≈8%), as highlighted in Figure 5. This distribution underscores the balanced yet persistent degradation pathways characteristic of long-haul operation.

Rain flow analysis was conducted for both the regional-haul and long-haul cycles, and the results were consistent with the degradation trends discussed earlier. To generate a normalized AST profile, a normalization factor is introduced to reduce the number of voltage fluctuations within each bin of the rainflow matrix. Initially, a normalization factor of 2 was applied; for example, a bin containing 240 fluctuations was reduced to 120. The entire matrix was scaled accordingly, and an AST profile was generated.

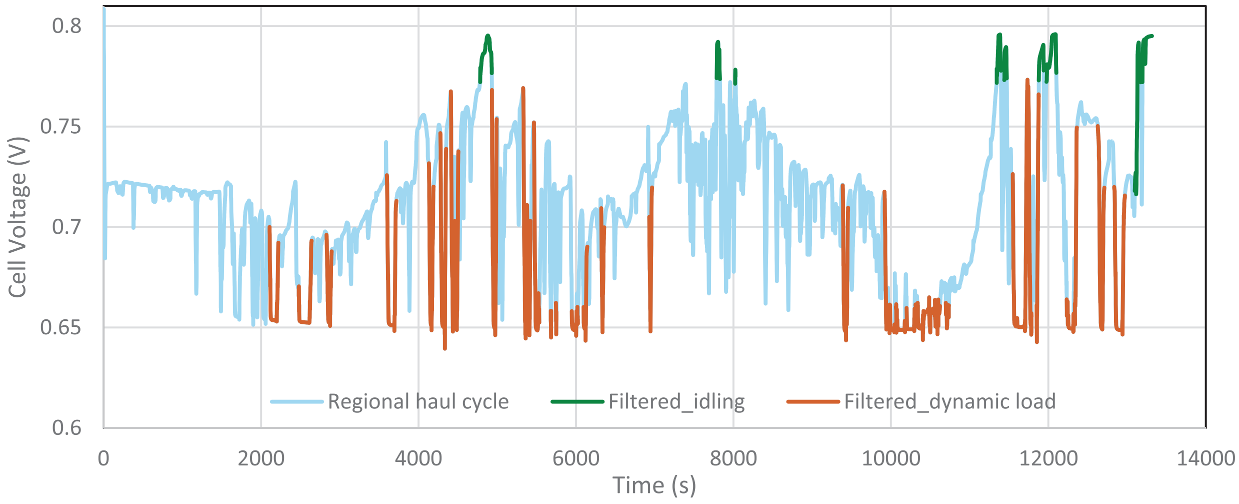

FIGURE 4 | The light blue driving cycle represents the regional-haul vehicle applications. In the cycle, degradation-critical segments are identified from dynamic load conditions (in orange) and idling phases (in green) and extracted to form a proportional AST.

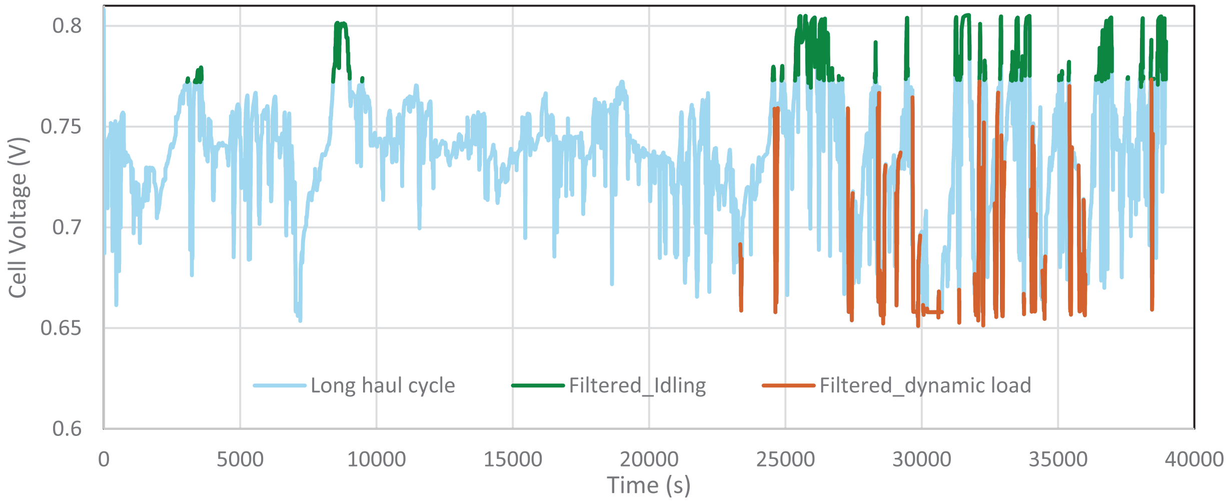

FIGURE 5 | The drive cycle shown in light blue represents the long-haul vehicle applications. In the cycle, degradation-critical segments are identified from dynamic load conditions (in orange) and idling phases (in green) and extracted to form a proportional AST.

However, comparison of degradation between the original drive cycle and the normalized AST revealed only a modest reduction in simulation time of approximately 10%. Subsequently, higher normalization factors ranging from 3 to 10 were evaluated. It was observed that a normalization factor of 5 resulted in a significant reduction in simulation time, achieving approximately 40% of time savings relative to the original cycle. Beyond this value, the reduction in time to estimate the degradation exhibited saturation behavior, with negligible additional improvement for higher factors. This saturation trend was consistently observed across multiple drive cycles. Therefore, a normalization factor of 5 is adopted in this study to represent the degradation behavior of the drive cycle. As illustrated in Figure 6, the rain flow matrix on the right corresponds to the regional-haul cycle, while the matrix on the left represents the matrix after normalization, where the fluctuations within each voltage bin have been rescaled. In the rain flow matrix, the rows denote the cycle minimum, while the columns represent the scan rate of the corresponding cycles. This binning approach allows the distribution of stressors across different voltage ranges to be visualized. The analysis reveals that in the regional-haul cycle, most of the stressors are concentrated in the low cycle minimum and low scan rates, indicating more frequent transitions within this operating window. In contrast, the long-haul cycle exhibits a broader distribution of stressors across the matrix but with more fluctuations in the mid-range voltages, reflecting its steady operation punctuated by fewer but longer transients. Importantly, the normalized AST demonstrates that the same extent of degradation observed in the regional-haul cycle can be reproduced in less than 40% of the original cycle duration, thereby accelerating aging processes while preserving the underlying degradation characteristics.

Table 2 summarizes the comparison between regional-haul and long-haul cycles under different testing approaches. The drive cycle durations are significantly reduced when proportional and normalized ASTs are applied. For the regional-haul case, the original drive cycle lasted 221 min, while the proportional and normalized cycles reduced the duration to 51 and 32 min,

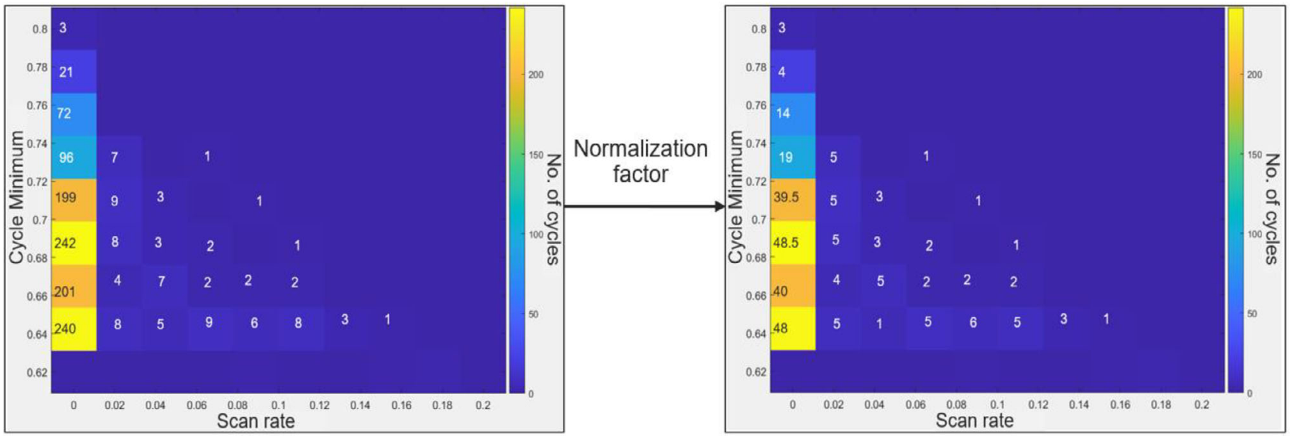

FIGURE 6 | The rain flow matrix of the regional haul cycle (right) is normalized by a factor of 5 to generate the reduced matrix (left). This process creates a shorter, accelerated cycle that consists of the same cycle minimum and scan rates of the original drive cycle.

respectively. Similarly, the long-haul cycle was shortened from 650 min in the original profile to 99 min in both the proportional and normalized cases. In the simulations, both cycles started with the same ECSA value of 261.7 cm^2/mgPt, and after simulating for 100 h, the regional-haul cycle exhibited more pronounced degradation compared to the long-haul cycle across all cases. For the baseline drive cycles, ECSA decreased to 251.7 cm^2/mgPt in the regional-haul case, while the long-haul cycle retained a higher value of 259.3 cm^2/mgPt. Under proportional AST conditions, the regional-haul case dropped further to 235.7 cm^2/mgPt, whereas the long-haul remained at 255.7 cm^2/mgPt. The strongest acceleration was observed under normalized AST, with the regional-haul ECSA decreasing to 228.7 cm^2/mgPt, compared to 254.3 cm^2/mgPt for the long-haul. This difference arises as the regional-haul cycle has high scan rates and more fluctuations at minimum voltage compared to the long-haul profile, which exposes the fuel cell to extended periods of low potentials and accelerates platinum dissolution. The long-haul cycle is characterized by steady operation at moderate potentials, with fewer transient fluctuations over time, thereby mitigating the severity of degradation. These observations clearly demonstrate that the nature of the vehicle speed profile strongly dictates the dominant degradation pathways within the MEA. Specifically, frequent idling and dynamic load variations intensify degradation through start–stop and high-potential mechanisms, whereas smoother and more stable driving conditions shift the degradation toward slower, support-related processes.

5 | Conclusions

The degradation behavior of a PEM fuel cell has been modeled and validated using experimental data obtained from electrochemical measurements (IL-TEM) conducted on a single cell. The degradation trends observed in the simulation show good agreement with the experimental results. Leveraging this model, a set of realistic ASTs was designed to replicate long-term degradation phenomena within a compressed timeframe.

Heavy-duty vehicle operating conditions, such as voltage cycling, idling, and high-load operations, are incorporated into the development of a proportional AST. In parallel, a normalized AST was derived using fatigue analysis techniques to account for the cyclic nature of fuel cell load profiles. Both AST methodologies are simulated across real-world driving scenarios, such as regional haul and long haul, to evaluate their effectiveness. Despite the operational differences, both derived ASTs significantly reduced the cycle time by approximately 85% and accelerated fuel cell degradation by approximately a factor of two. This consistent acceleration rate across different drive cycles highlights the adaptability of the proposed AST frameworks. Furthermore, these two approaches preserve realistic vehicle operating scenarios, and they can be reflected in predicting vehicle degradation behavior. Their ability to significantly shorten prediction time without compromising physical relevance makes them capable compared to state-of-the-art AST protocols for estimating long-term PEMFC performance and lifetime.

In future work, the degradation model will be extended to incorporate membrane-specific failure mechanisms driven by variations in temperature and humidity. In addition, the developed AST protocols, along with representative drive cycles, can be implemented in single-cell experimental setups to further validate the simulation framework and enhance its predictive capability.

Acknowledgments

The Competence Centre TechForH2 is hosted by Chalmers University of Technology and is financially supported by the Swedish Energy Agency (P2021-90268) and the member companies Volvo, Scania, Siemens Energy, GKN Aerospace, Power Cell, Oxeon, RISE, Stena Rederier AB, Johnsson Matthey, and Insplorion.

Conflicts of Interest

The authors declare no conflicts of interest.

References

1. New Energy and Industrial Technology Development Organization (NEDO), *Fuel Cell and Hydrogen Technology Development Roadmap: Fuel Cell Roadmap for FCVs/HDVs* 2024.

2. R. Petrone, D. Hissel, M. C. Péra, D. Chamagne, and R. Gouriveau, "Accelerated Stress Test Procedures for PEM Fuel Cells Under Actual

Load Constraints: State-of-the-Art and Proposals," *International Journal of Hydrogen Energy* 40 (2015): 12489–12505, https://doi.org/10.1016/j.ijhydene.2015.07.026.

3. K. Xu, X. Zhao, X. Hu, et al., "The Review of the Degradation Mechanism of the Catalyst Layer of the Membrane Electrode Assembly in the Proton Exchange Membrane Fuel Cell," *IOP Conference Series: Earth and Environmental Science* 558 (2020): 052041.

4. P. Pei, X. Fu, Z. Zhu, P. Ren, and D. Chen, "Activation of Polymer Electrolyte Membrane Fuel Cells: Mechanisms, Procedures, and Evaluation," *International Journal of Hydrogen Energy* 47, no. 59 (2022): 24897–249157, https://doi.org/10.1016/j.ijhydene.2022.05.228.

5. J. Sim, M. Kang, K. Min, E. Lee, and J.-Y. Jyoung, "Effects of Carbon Corrosion on Proton Exchange Membrane Fuel Cell Performance Using Two Durability Evaluation Methods," *Renewable Energy* 190 (2022): 959–970, https://doi.org/10.1016/j.renene.2022.04.015.

6. Z. Penga, G. Radica, F. Barbir, and P. Eckert, *Degradation Mechanisms in Automotive Fuel Cell Systems* (Fuel Cells and Hydrogen Joint Undertaking, 2017).

7. E. Pahon, D. Hissel, and N. Yousfi-Steiner, "A Review of Accelerated Stress Tests Dedicated to Proton Exchange Membrane Fuel Cells—Part I: Fuel Cell Component Level," *Journal of Power Sources* 546 (2022): 231895, https://doi.org/10.1016/j.jpowsour.2022.231895.

8. F. A. De Bruijn, V. A. T. Dam, and G. J. M. Janssen, "Review: Durability and Degradation Issues of Pem Fuel Cell Components," *Fuel Cells* 8 (2008): 3–22, https://doi.org/10.1002/fuce.200700053.

9. E. Wallnöfer-Ogris, F. Poimer, R. Köll, M.-G. Macherhammer, and A. Trattner, "Main Degradation Mechanisms of Polymer Electrolyte Membrane Fuel Cell Stacks—Mechanisms, Influencing Factors, Consequences, and Mitigation Strategies," *International Journal of Hydrogen Energy* 50 (2023): 1159–1182, https://doi.org/10.1016/j.ijhydene.2023.06.215.

10. V. Patil, P. V. Reshmi, and S. Prajna, "Degradation Mechanisms in Pem Fuel Cells: A Brief Review," *Materials Today: Proceedings* (2023), https://doi.org/10.1016/j.matpr.2023.03.603.

11. A. Haragirimana, N. Li, Z. Hu, and S. Chen, "A Facile, Effective Thermal Crosslinking to Balance Stability and Proton Conduction for Proton Exchange Membranes Based on Blend Sulfonated Poly(ether ketone)/Sulfonated Poly(arylene ether sulfone)," *International Journal of Hydrogen Energy* 46, no. 29 (2021): 15866–15877, https://doi.org/10.1016/j.ijhydene.2021.02.022.

12. X.-Z. Yuan, H. Li, S. Zhang, J. Martin, and H. Wang, "A Review of Polymer Electrolyte Membrane Fuel Cell Durability Test Protocols," *Journal of Power Sources* 196, no. 22 (2011): 9107–9116, https://doi.org/10.1016/j.jpowsour.2011.07.082.

13. A. Bisello, E. Colombo, A. Baricci, et al., "Mitigated Start-Up of PEMFC in Real Automotive Conditions: Local Experimental Investigation and Development of a New Accelerated Stress Test Protocol," *Journal of the Electrochemical Society* 168 (2021): 054501, https://doi.org/10.1149/1945-7111/abf77b.

14. S. R. Dhanushkodi, S. Kundu, M. W. Fowler, and M. D. Pritzker, "Study of the Effect of Temperature on Pt Dissolution in Polymer Electrolyte Membrane Fuel Cells via Accelerated Stress Tests," *Journal of Power Sources* 245 (2014): 1035–1045, https://doi.org/10.1016/j.jpowsour.2013.07.016.

15. R. Mukundan, A. M. Baker, A. Kusoglu, et al., "Membrane Accelerated Stress Test Development for Polymer Electrolyte Fuel Cell Durability Validated Using Field and Drive Cycle Testing," *Journal of the Electrochemical Society* 165 (2018): F3085–F3093, https://doi.org/10.1149/2.0101806jes.

16. N. Macauley, D. D. Papadias, J. Fairweather, et al., "Carbon Corrosion in PEM Fuel Cells and the Development of Accelerated Stress Tests," *Journal of the Electrochemical Society* 165 (2018): F3148–F3160, https://doi.org/10.1149/2.0061806jes.

17. G. Tsotridis, A. Pilenga, G. De Marco, and T. Malkow, *EU Harmonised Test Protocols for PEMFC MEA Testing in Single Cell Configuration for Automotive Applications* (Publications Office of the European Union, 2015).

18. C. Rabissi, M. Zago, F. Bresciani, P. Gazdzicki, and A. Casalegno, "A Novel Accelerated Stress Test for a Representative Enhancement of Cathode Degradation in Direct Methanol Fuel Cells," *Energies* 16, no. 7 (2023): 3226, https://doi.org/10.3390/en16073226.

19. L. Xu, J. Li, U. Reimer, et al., "Methodology of Designing Durability Test Protocol for Vehicular Fuel Cell System Operated in Soft Run Mode Based on Statistic Results of On-Road Data," *International Journal of Hydrogen Energy* 42 (2017): 29840–29851, https://doi.org/10.1016/j.ijhydene.2017.10.060.

20. R. K. F. Della Bella, B. M. Stühmeier, and H. A. Gasteiger, "Universal Correlation Between Cathode Roughness Factor and H_2/Air Performance Losses in Voltage Cycling-Based Accelerated Stress Tests," *Journal of the Electrochemical Society* 169 (2022): 044528, https://doi.org/10.1149/1945-7111/ac67b8.

21. M. Schüttoff, C. Wachtel, R. Schlumberger, F. Wilhelm, J. Scholta, and M. Hölzle, "Development of Accelerated Durability Test Protocols for Polymer Electrolyte Membrane Fuel Cell Stacks Under Realistic Operating Conditions," *Fuel Cells* 24, no. 5 (2024): e202300263, https://doi.org/10.1002/fuce.202300263.

22. K. Collins, R. Der Wartanian, Y. Hou, S. K. Ayyagari, and B. P. Khatri, "Using Big Data to Analyze Long-Haul vs Regional-Short-Haul Trips for Medium- and Heavy-Duty Vehicles," *Data in Brief* 59 (2025): 111370, https://doi.org/10.1016/j.dib.2025.111370.

23. M. Mayur, S. Strahl, A. Husar, and W. G. Bessler, "A Multi-Timescale Modeling Methodology for PEMFC Performance and Durability in a Virtual Fuel Cell Car," *International Journal of Hydrogen Energy* 40, no. 46 (2015): 16466–16476, https://doi.org/10.1016/j.ijhydene.2015.09.152.

24. A. Kneer and N. Wagner, "A Semi-Smpirical Catalyst Degradation Model Based on Voltage Cycling Under Automotive Operating Conditions in PEM Fuel Cells," *Journal of the Electrochemical Society* 166 (2019): F120–F127, https://doi.org/10.1149/2.0641902jes.

25. L. Castanheira, W. O. Silva, F. H. B. Lima, A. Crisci, L. Dubau, and F. Maillard, "Carbon Corrosion in Proton-Exchange Membrane Fuel Cells: Effect of the Carbon Structure, the Degradation Protocol, and the Gas Atmosphere," *ACS Catalysis* 5, no. 4 (2015): 2184–2194, https://doi.org/10.1021/cs501973j.

26. Y. Li, K. Moriyama, W. Gu, S. Arisetty, and C. Y. Wang, "A One-Dimensional Pt Degradation Model for Polymer Electrolyte Fuel Cells," *Journal of the Electrochemical Society* 162 (2015): F834–F842, https://doi.org/10.1149/2.0101508jes.

27. E. F. Holby, W. Sheng, Y. Shao-Horn, and D. Morgan, "Pt Nanoparticle Stability in PEM Fuel Cells: Influence of Particle Size Distribution and Crossover Hydrogen," *Energy and Environmental Science* 2 (2009): 865, https://doi.org/10.1039/b821622n.

28. E. F. Holby and D. Morgan, "Application of Pt Nanoparticle Dissolution and Oxidation Modeling to Understand Degradation in PEM Fuel Cells," *Journal of the Electrochemical Society* 159 (2012): B578–B591, https://doi.org/10.1149/2.011204jes.

29. K. G. Gallagher and T. F. Fuller, "Kinetic Model of the Electrochemical Oxidation of Graphitic Carbon in Acidic Environments," *Physical Chemistry Chemical Physics* 11 (2009): 11557, https://doi.org/10.1039/b915478g.

30. J. Zhao, Z. Tu, and S. H. Chan, "Carbon Corrosion Mechanism and Mitigation Strategies in a Proton Exchange Membrane Fuel Cell (PEMFC): A Review," *Journal of Power Sources* 488 (2021): 229434, https://doi.org/10.1016/j.jpowsour.2020.229434.

31. S. R. Dhanushkodi, S. Kundu, M. W. Fowler, and M. D. Pritzker, "Use of Mechanistic Carbon Corrosion Model to Predict Performance Loss in Polymer Electrolyte Membrane Fuel Cells," *Journal of Power Sources* 267 (2014): 171–181, https://doi.org/10.1016/j.jpowsour.2014.05.041.

32. D. Garcia-Sanchez, T. Morawietz, P. G. Da Rocha, R. Hiesgen, P. Gazdzicki, and K. A. Friedrich, "Local Impact of Load Cycling on

Degradation in Polymer Electrolyte Fuel Cells," *Applied Energy* 259 (2020): 114210, https://doi.org/10.1016/j.apenergy.2019.114210.

33. L. Xu, J. Li, U. Reimer, et al., "Methodology of Designing Durability Test Protocol for Vehicular Fuel Cell System Operated in Soft Run Model Based on Statistical Results of On-Road Data," *International Journal of Hydrogen Energy* 42, no. 50 (2017): 29840–29851, https://doi.org/10.1016/j.ijhydene.2017.10.060.

34. P. Thiele, Y. Yang, S. Dirkes, M. Wick, and S. Pischinger, "Realistic Accelerated Stress Tests for PEM Fuel Cells: Test Procedure Development Based on Standardized Automotive Driving Cycles," *International Journal of Hydrogen Energy* 52 (2023): 1065–1080, https://doi.org/10.1016/j.ijhydene.2023.08.292.

35. M. Yue, Z. Li, R. Roche, S. Jemei, and N. Zerhouni, "Degradation Identification and Prognostics of Proton Exchange Membrane Fuel Cell Under Dynamic Load," *Control Engineering Practice* 118 (2022): 104959, https://doi.org/10.1016/j.conengprac.2021.104959.

36. E. Hantoosh Zadeh, M. Shojayian, and E. Kjeang, "Impact of Dwell Time and Lower Potential Limit During Voltage Cycling on PEM Fuel Cells Catalyst Durability," in *ECS Meeting Abstracts* MA2023-02 (2023): 1774.

37. M. Zatoń, J. Rozière, and D. J. Jones, "Current Understanding of Chemical Degradation Mechanisms of Perfluoro Sulfonic Acid Membranes and Their Mitigation Strategies: A Review," *Sustainable Energy & Fuels* 1 (2017): 409–438, https://doi.org/10.1039/C7SE00038C.

38. J. Shan, P. Gazdzicki, R. Lin, M. Schulze, and K. A. Friedrich, "Local Resolved Investigation of Hydrogen Crossover in Polymer Electrolyte Fuel Cell," *Energy* 128 (2017): 357–365, https://doi.org/10.1016/j.energy.2017.03.104.

39. H. Li, J. You, X. Cheng, et al., "Unraveling the Effects of Carbon Corrosion on Oxygen Transport Resistance in Low Pt Loading Proton Exchange Membrane Fuel Cells," *ACS Applied Materials Interfaces* 16 (2024): 540–554, https://doi.org/10.1021/acsami.3c13450.

40. X. Cheng, G. Wei, C. Wang, S. Shen, and J. Zhang, "Experimental Probing of Effects of Carbon Support on Bulk and Local Oxygen Transport Resistance in Ultra-Low Pt PEMFCs," *International Journal of Heat and Mass Transfer* 164 (2021): 120549, https://doi.org/10.1016/j.ijheatmasstransfer.2020.120549.

41. M. A. Schmid, J. Kaczerowski, F. Wilhelm, J. Scholta, B. Müller, and M. Hölzle, "Aging Effects Observed in Automotive Fuel Cell Stacks by Applying a New Realistic Test Protocol and Humidity Control," *Fuel Cells* 24, no. 5 (2024): e202300227, https://doi.org/10.1002/fuce.202300227.

42. A.-C. Scherzer, P. Schneider, M. Klingele, N. Zamel, and D. Gerteisen, "Simulating Morphology and Degradation of PEMFC Cathode Catalyst Layers With Porous Carbon Supports: Part II. Effect of Ionomer and Relative Humidity on Catalyst Degradation," *Journal of the Electrochemical Society* 172 (2025): 074504, https://doi.org/10.1149/1945-7111/adc8d9.

43. K. Xu, Q. Di, F. Sun, M. Chen, and H. Wang, "Degradation Mechanism Analysis of Substrate and Microporous Layer of Gas Diffusion Layer in Proton Exchange Membrane Fuel Cell," *Fuel* 358 (2024): 130198, https://doi.org/10.1016/j.fuel.2023.130198.

44. Y. L. Lee and T. Tjhung, "Rainflow Cycle Counting Techniques," in *Metal Fatigue Analysis Handbook* (Elsevier Inc., 2012), 89–114.

45. V. Shokhen, L. Strandberg, M. Skoglundh, and B. Wickman, "Fuel Cell Electrode Degradation Followed by Identical Location Transmission Electron Microscopy," *Journal of Materials Chemistry A* 11, no. 39 (2023): 21029–21035, https://doi.org/10.1039/D3TA01303K.